



OPEN

Insulator-to-half metal transition and enhancement of structural distortions in $\text{Lu}_2\text{NiIrO}_6$ double perovskite oxide via hole-doping

Safdar Nazir

Using density functional theory calculations, we found that recently high-pressure synthesized double perovskite oxide $\text{Lu}_2\text{NiIrO}_6$ exhibits ferrimagnetic (FiM) Mott-insulating state having an energy band gap of 0.20 eV which confirms the experimental observations (Feng et al. in *Inorg Chem* 58:397–404, 2019). Strong antiferromagnetic superexchange interactions between high-energy half-filled $\text{Ni}^{+2} - e_g^2 \uparrow$ and low-energy partially filled $\text{Ir}^{+4} t_{2g}^3 \uparrow t_{2g}^2 \downarrow$ orbitals, results in a FiM spin ordering. Besides, the effect of 3d transition metal (TM = Cr, Mn, and Fe) doping with 50% concentration at Ni sites on its electronic and magnetic properties is explored. It is established that smaller size cation-doping at the B site enhances the structural distortion, which further gives strength to the FiM ordering temperature. Interestingly, our results revealed that all TM-doped structures exhibit an electronic transition from Mott-insulating to a half-metallic state with effective integral spin moments. The admixture of Ir 5d orbitals in the spin-majority channel are mainly responsible for conductivity, while the spin minority channel remains an insulator. Surprisingly, a substantial reduction and enhancement of spin moment are found on non-equivalent Ir and oxygen ions, respectively. This leads the Ir ion in a mixed-valence state of +4 and +5 in all doped systems having configurations of $5d^5 (t_{2g}^3 \uparrow t_{2g}^2 \downarrow)$ and $5d^4 (t_{2g}^2 \uparrow t_{2g}^2 \downarrow)$, respectively. Hence, the present work proposes that doping engineering with suitable impurity elements could be an effective way to tailor the physical properties of the materials for their technological potential utilization in advanced spin devices.

Recently, double perovskite oxides (DPO) having a chemical formula $\text{ABB}'\text{O}_6$ (A = alkaline earth or rare earth metal atoms and $\text{BB}' = 3d$ and $4/5d$ transition metals such as B = Fe, Cr, Mn, Co, and Ni; $\text{B}' = \text{Mo, Re, Os, Ir, and W}$) have been attracting a lot of attention due to their unusual physical properties such as large magnetoresistance at or above room temperature^{1–6}, high-temperature ferromagnetism (FM)/ferrimagnetism (FiM)^{7–10}, half-metallicity^{6,11–14}, FM/FiM Mott-insulator^{15–18}, multiferroicity¹⁹, exchange bias²⁰, and magneto-dielectricity²¹. Particularly, a half-metallic (HM) state in $\text{Sr}_2\text{FeMoO}_6$ ^{1,7,22} and $\text{Sr}_2\text{FeReO}_6$ ^{2,23,24} (i.e., one spin channel exhibits a conducting nature while the other is insulator or semiconductor) having Curie temperature (T_C) of 400–415 K is found, which displayed novel applications for spintronics perspective^{25,26}. In most of the experiments, it is analyzed that HM is FM such as $\text{La}_{1-x}\text{Sr}_x\text{MnO}_3$ ²⁷ and few are HM FiMs or highly spin-polarized like $\text{Sr}_2\text{CrReO}_6$ having a T_C of 635 K^{8,9,28,29}. The highest T_C of 725 K is observed in $\text{Sr}_2\text{CrOsO}_6$ with the magnetic moment of 1.92 to $2.04 \mu_B$ ^{12,15,16}. Very recently, Feng et al.¹⁸, synthesized disordered monoclinic $\text{Lu}_2\text{NiIrO}_6$ (LNIO) DPO under high-pressure (6 GPa) and high-temperature (1300 °C), where authors observed a FiM Mott-insulating state having a highest T_C of 207 K among the disordered DPOs. A FiM Mott-insulating ground state in the LNIO was also verified by first-principle calculations, where a strong superexchange AFM coupling between Ni and Ir ions is energetically favorable³⁰. A small and large energy band gaps (E_g) of 0.20 and 2.25 eV exist in the spin-majority and spin-minority channels, respectively. Hence, due to a small energy gap and high T_C among the Ir-based DPOs, LNIO could be an essential material in the designing of hard magnetic memory devices by tailoring its properties. The above mention properties of the DPOs have been stimulated the researchers to synthesize or predict new materials with improved electronic and magnetic properties.

As it is experimentally and theoretically established that DPOs are considered beneficial candidates for electron and hole-doping at A or B site, aiming to obtain optimized physical properties that were not present in their undoped form^{31–47}. For example, in a widely studied $\text{Sr}_2\text{FeMoO}_6$ DPO, electron doping which is obtained by partial replacement of Sr^{+2} with $\text{La}^{+3}/\text{Nd}^{+3}$ results in the enhancement of T_C ^{31–34}. Interestingly, the electrical

Department of Physics, University of Sargodha, Sargodha 40100, Pakistan. email: safdar.nazir@uos.edu.pk

resistivity of the $\text{Sr}_2\text{FeMoO}_6$ system decreases when a Sulfur ion is doped at oxygen site and FiM or AFM spin ordering-like behavior arise at low temperatures⁴¹. Similarly, Geprags et al.³⁵, experimentally observed that electron doping in the La_2CrWO_6 FiM DPO usually enhances the T_C . Blasco et al.³⁷, experimentally observed that magnetic transition temperature increases with the increase of La doping at Sr site in $\text{Sr}_2\text{CrMoO}_6$. Along with this, La^{+3} doping at Ca^{+2} site in $\text{Ca}_2\text{FeIrO}_6$ results in the modulation of microscopic magnetic coupling, which further leads to the magnetic phase transition from AFM to FiM³⁶. Similarly, an AFM to FiM spin ordering transition is observed in $(\text{Ca},\text{Sr})_2\text{FeIrO}_2$ system due to La^{+3} -doping and authors claimed that changes in the microscopic magnetic interaction may be associated with the mixed-valence state of Ir³⁸. In a similar fashion, $\text{Pr}_{2-x}\text{Sr}_x\text{MgIrO}_6$ system exhibits a transition from Mott-insulating to HM AFM state at $x = 1.0$, where Ir-ion remains in mixed-valence states of +4, +4/ +5, and +5 for $\text{Pr}_2\text{MgIrO}_6$, $\text{Pr}_{1.5}\text{Sr}_{0.5}\text{MgIrO}_6$, and PrSrMgIrO_6 samples, respectively⁴⁵. Moreover, Coutrim et al., experiments show that variations of the magnetic coupling between Co and Ir ions in $\text{La}_2\text{CoIrO}_6$ are due to a change of their valence, when La is replaced with Ca ion having a concentration of $0 \leq \text{Ca} \leq 1.2$ ⁴⁰. It is also observed that net magnetization and T_C decreases when Ca-doped in $\text{La}_2\text{CoIrO}_6$. However, the magnetization of $\text{Sr}_2\text{MnMoO}_6$ compound increases at a very low concentration (≤ 0.15) of Bi doping at Sr site, which also illustrates an AFM coupling between Mn^{+2} and Mo^{+5} ions and results in a FiM spin ordering⁴².

From a theoretical point of view, it is found that hole-doping (i.e., Sr^{+2} -doping at La^{+3} site) in a FiM La_2VMnO_6 ($\text{La}_{2-x}\text{Sr}_x\text{VMnO}_6$) leads the system to HM state³⁹. It is also demonstrated that holes remain in the V 3d orbitals for $x = 0.5$ and 1.0 and thenceforth, lie in the Mn 3d orbitals for $x = 1.5$ and 2.0. Alike, the hole-doping (i.e., Na^{+1} -doping at Pb^{+2} site) in a C-type AFM Mott-insulator $\text{Pb}_2\text{FeOsO}_6$ ($\text{Pb}_{2-x}\text{Na}_x\text{FeOsO}_6$) DPO results in an HM FiM state, and the holes produced by Na doping resides in the Os 5d orbitals⁴³. Lv et al., first-principles calculations exhibited that electron doping (i.e., La^{+3} -doping at Ba^{+2} site) leads a transition from Mott-insulator AFM to HM AFM in $\text{Ba}_{2-x}\text{La}_x\text{MnMoO}_6$ for $x \leq 1.0$ and then to a metallic AFM state for $x = 1.5$ and 2.0⁴⁸. It is also predicted that extra electrons go to the Mo 4d orbitals, which are responsible for metallicity in these doped systems. Very recently, Bhandari et al.⁴⁷, theoretically demonstrated that electron doping at B site (i.e., 50% Ni-doping at Cr site) in a FiM Mott-insulator $\text{Ca}_2\text{CrOsO}_6$ gives rise to a nearly compensated HM state which has potential applications for spintronic devices. In this case, Ni is in a +2 state with $3d^8$ configurations and when it is replaced with Cr of charge of +3 having a configuration of $3d^3$, therefore, five extra electrons added to the system which results in an HM state.

In this regard, this doping strategy in recently synthesized FiM Mott-insulator LNIO DPO¹⁸ could be very beneficial for its utilization in spintronic devices because of the low/high energy band gap of 0.20/2.25 eV in the spin-majority/spin-minority channel³⁰ with a higher T_C of 207 K among the disorder DPOs. Therefore, we explored a possibility to produce the HM materials via hole-doping engineering, that is, to introduce one 3d TM = Cr, Mn, and Fe of impurity ions at one of the B-site atom (i.e., which is also a 3d TM site: Ni site) in LNIO system using first-principles electronic structure calculations. Hence, the doping concentration of TM-doped atoms is 50% in the stable solid solution. Therefore, the TM-doped LNIO structures are most likely referred to as an alloy. These potential elements show HM nature having absolute magnetic moments with improved FiM ordering temperature.

Results and discussion

Structural properties. LNIO crystallizes in the monoclinic structure with space group No. 14 ($P2_1/n$) and the experimental lattice parameters are $a = 5.21431$, $b = 5.63533$, and $c = 7.53905$ Å with $\beta = 90.1834^\circ$ ¹⁸. The Lu, Ni, Ir, O1, O2, and O3 ions occupy the Wyckoff positions $4e(0.9755, 0.07858, 0.2507)$, $2c(0.5, 0, 0.5)$, $2b(0.5, 0, 0)$, $4e(0.1372, 0.4484, 0.2521)$, $4e(0.6820, 0.3061, 0.0592)$, and $4e(0.1786, 0.1880, 0.9396)$, respectively. Our prior DFT calculations³⁰ and Feng et al. experiment¹⁸ exhibit that Mott-insulating FiM state is more energetically stable than that of FM and AFMs structures in pristine LNIO, because AFM superexchange coupling between Ni and Ir are strongly favorable at the diagonals. Moreover, it is found that the next magnetic state close to the FiM ground state is FM³⁰, therefore, we considered the FM and different FiM structure for further doping engineering in the present study. The schematic representation of crystal structures of $\text{Lu}_2\text{Ni}_{0.5}\text{TM}_{0.5}\text{IrO}_6$ in an FM, FiM-I, FiM-II, FiM-III, and FiM-IV spin orderings are shown in Fig. 1a–e, respectively. In an FM spin ordering, Ni, TM, and Ir ions spins are parallel (Fig. 1a), while they are anti-parallel within both in-plane and out-of-plane directions in FiM-I state (Fig. 1b). In the case of FiM-II structure, Ni, TM, and one Ir ion spins are parallel to each other (i.e., ferromagnetically coupled) and the second Ir ion is anti-parallel to all of them as shown in Fig. 1c. For FiM-III spin ordering, TM and both Ir ions spins are anti-align than that of Ni (Fig. 1d), while both Ir and Ni ions spins are aligned with each other than that of TM in FiM-IV structure (Fig. 1e). Here, it is very important to note that only ordered TM-doped structures are considered likewise undoped one. However, a disordered between Ni and TM ions may exist due to a small difference in their size or charge which highly demands its experimental verification.

Structural stability and magnetic ground state. To estimate the relative structural stability of TM-doped LNIO systems, formation energy (E_f) in each case is calculated as:

$$E_f = E_{\text{doped}} - E_{\text{undoped}} - \mu_{\text{TM}} + \mu_{\text{Ni}} \quad (1)$$

where E_{doped} and E_{undoped} refers to the total energy of TM-doped and undoped LNIO DPO, respectively. μ_{TM} and μ_{Ni} are the chemical potentials of the TM and Ni atoms, which are the total energies of the most stable low-temperature phases of the bulk TM and Ni (E_{TM} and E_{Ni}), respectively. The calculated values of E_f for Cr-, Mn-, and Fe-doped LNIO materials are -0.52 , -1.21 , and -1.65 eV, respectively (also listed in Table 1). The “−” values of E_f for all TM-doped systems indicate that they are thermodynamically stable and can be easily

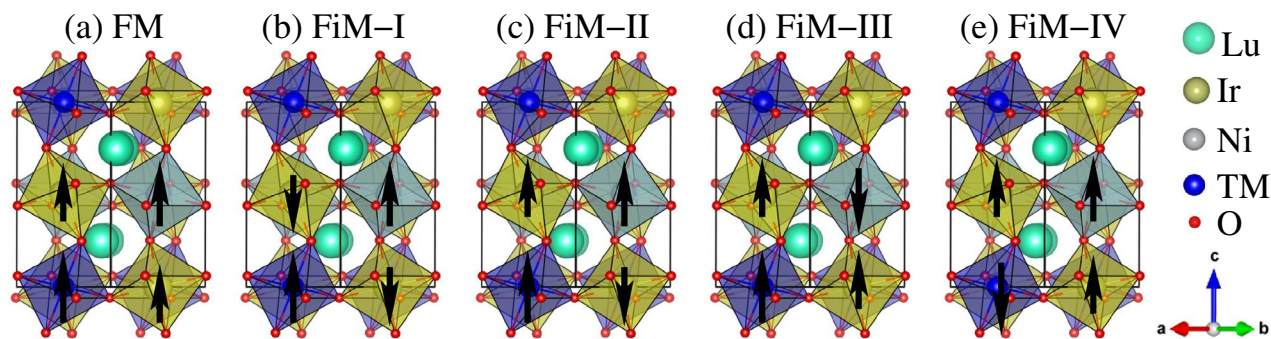


Figure 1. Schematic representation of the double perovskite structures of $\text{Lu}_2\text{Ni}_{0.5}\text{TM}_{0.5}\text{IrO}_6$ (TM = Cr, Mn, and Fe) in (a) ferromagnetic (FM), (b) ferrimagnetic (FiM-I), (c) FiM-II, (d) FiM-III, and (e) FiM-IV spin ordering. The tilted octahedral surroundings of the Ni, TM, and Ir with oxygen atoms are visualized in light grey, light blue, and light green colored polyhedron, respectively. The a , b , and c -axes are along the crystallographic x , y , and z -directions, respectively.

TM	E_f	ΔE_1	ΔE_2	ΔE_3	ΔE_4	T_{C1}	E_g	$m_{tot./u.c.}$	$m_{tot./f.u.}$	m_{Ni}	m_{TM}	m_{Ir1}	m_{Ir2}	m_{O1}	m_{O2}	m_{O3}
Undop.	–	28.3	25.5	17.8	17.5	219	0.20	1.90	0.95	1.66	1.66	–0.54	–0.54	–0.01	–0.03	–0.02
Cr	–0.52	37.7	35.5	33.3	31.9	292	HM	4.00	2.00	1.66	2.66	–0.09	–0.39	–0.09	–0.39	–0.03
Mn	–1.21	33.8	31.2	30.5	28.7	261	HM	5.00	2.50	1.69	3.80	–0.16	–0.41	–0.16	–0.41	–0.02
Fe	–1.65	30.5	29.2	28.9	–13.8	236	HM	6.00	3.00	1.67	4.11	–0.05	–0.42	–0.06	–0.42	–0.09

Table 1. Calculated formation energy (E_f) in eV, magnetic energy differences: $\Delta E_1 = E_{FM} - E_{FiM-I}$, $\Delta E_2 = E_{FM} - E_{FiM-II}$, $\Delta E_3 = E_{FM} - E_{FiM-III}$, and $\Delta E_4 = E_{FM} - E_{FiM-IV}$ in meV, FiM ordering temperature (T_{C1}) in K, and energy band gap (E_g) in eV for $\text{Lu}_2\text{Ni}_{0.5}\text{TM}_{0.5}\text{IrO}_6$ (TM = Cr, Mn, and Fe) double perovskite oxides. The “–” and “+” signs in E_f and ΔE show that doped crystal structure and FiM spin ordering are energetically stable, respectively. Moreover, “HM” in the E_g column represents the half-metallic nature of the system along with total spin moments per unit cell ($m_{tot./u.c.}$) as well as per formula unit ($m_{tot./f.u.}$) and partial spin moments on Ni (m_{Ni}), TM (m_{TM}), Ir (m_{Ir}), and O (m_O) ions.

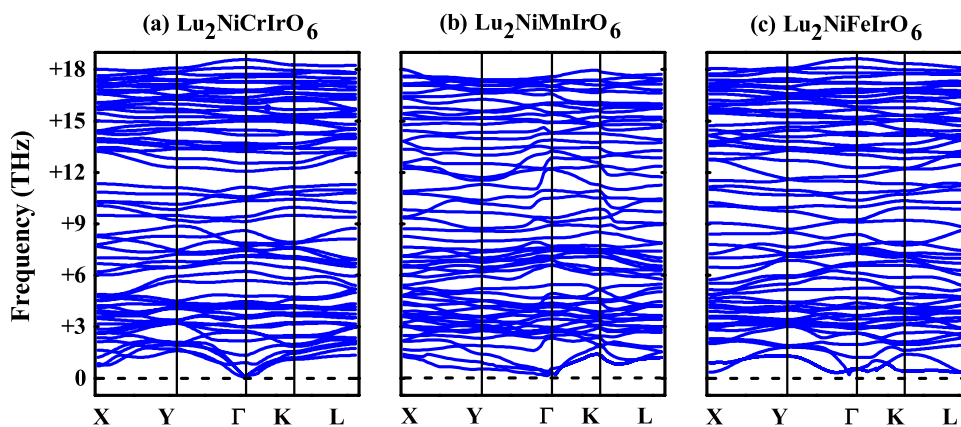


Figure 2. Calculated phonon dispersion band structures for (a) Cr-, (b) Mn-, and (c) Fe-doped $\text{Lu}_2\text{NiIrO}_6$ double perovskite oxides.

synthesized. Furthermore, the phonon dispersion calculations have been performed to check the dynamic stability of doped systems. The computed phonon dispersion bands are plotted in Fig. 2a–c for Cr-, Mn-, and Fe-doped LNIO structures, respectively. The phonon dispersions show a set of 60 phonon branches owing to the presence of 20 atoms per primitive cell. The higher frequency manifold is mainly attributed to vibrations of oxygen atoms which are dispersive and well separated in the higher energy regime as compared to the atomic species⁴⁹. The absence of the imaginary frequencies in all TM-doped systems, which provides real evidence of the structures dynamic stability. The lower manifold from 0 to +6 THz consists of the acoustic modes (24 phonon branches for each case) but it can also be noticed that some of the modes have strongly mixed character, which may lead the systems to metallicity.

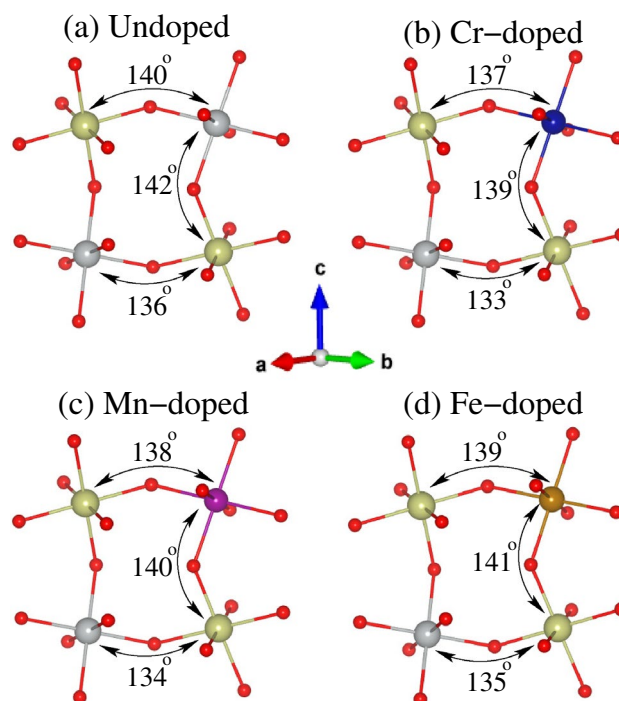


Figure 3. A crystallographic view of the crystal structure of (a) undoped, (b) Cr-doped, (c) Mn-doped, and Fe-doped $\text{Lu}_2\text{NiIrO}_6$ double perovskite oxides along with DFT relaxed three peculiar Ni(TM)-O-Ir bond angles. The a , b , and c -axes are along the crystallographic x , y , and z -directions, respectively.

Next, the energetically favorable magnetic ground state in undoped and doped TM-doped LNIO DPO is examined by comparing the total energies of FM with different FiM structures as $\Delta E_1/\Delta E_2/\Delta E_3/\Delta E_4 = E_{FM} - E_{FiM-I}/E_{FM} - E_{FiM-II}/E_{FM} - E_{FiM-III}/E_{FM} - E_{FiM-IV}$. The computed values of ΔE_1 , ΔE_2 , ΔE_3 , and ΔE_4 are listed in Table 1. The “-” and “+” signs of ΔE means that FM and FiM spin ordering are more energetically stable, respectively. Our calculations show that FiM-I spin ordering in the undoped and all doped structures are energetically favorable (i.e., ΔE_1 is the ground state in each case) than that of FM and remaining FiM structures. This means that Ni and TM ion spins want to remain parallel with each other at the diagonal site, but prevail anti-parallel with Ir in both in-plane and out-of-plane. From ΔE_1 , the FiM ordering temperature T_{C1} in each doped case is computed as $\frac{2/3 \cdot \Delta E_1}{k_B}$, where k_B is the Boltzmann constant. The calculated T_{C1} for undoped, Cr, Mn, and Fe-doped LNIO materials are 219, 369, 339, and 360 K (also listed in Table 1) corresponds to ΔE_1 in each case, respectively. It is also important to note that our computed T_C of 219 K in undoped LNIO material is very close to the experimentally observed value of 207 K¹⁸. Interestingly, present calculations predicted that T_C enhanced when one of the Ni ions is replaced with TM having the highest $T_{C1} = 292$ K for Cr-doped material. This means that the structural distortion increases with the TM-doping as compared to the undoped one. As, FiM-I spin ordering is the energetically favorable magnetic ground state in the undoped and all TM-doped LNIO structures, therefore, for further investigations only FiM-I magnetic structure is taken into account in all cases.

Octahedral distortion. It is previously established that deviation of $3d$ -O- $5d$ bond angles from the perfect geometry of the high cubic symmetry structure (180°) in a distorted DPOs lead to a strong AFM superexchange coupling between magnetic ions, which results in a FiM ordering^{46,50–54} and large structural distortions enhance the FiM ordering temperature^{55–57}. Therefore, we displayed the DFT relaxed three peculiar TM-O-Ir bond angles on TMO_6 and IrO_6 octahedron for undoped, Cr-doped, Mn-doped, and Fe-doped LNIO materials in Fig. 3a–d, respectively. The calculated Ni-O1-Ir/Ni-O2-Ir/Ni-O3-Ir bond angles of $136^\circ/142^\circ/140^\circ$ in undoped LNIO (see Fig. 3a) are in a good agreement with the experimentally observed values of $135.4^\circ/142.5^\circ/140.8^\circ$ ¹⁸. Surprisingly, our results show that the substitution of smaller TM cations into Ni-site produced a significant structural distortion which further affects the electronic and magnetic properties. As the Cr-doped LNIO system exhibits large structural distortions (i.e., smaller bond angles) than that of undoped and other doped systems, compare the bond angles magnitudes in Fig. 3b with that of Fig. 3a,c,d, respectively. This usually demands a higher energy difference between the different magnetic structures, which results in a higher T_C as displayed in Table 1.

Electronic properties. To explicitly display the TM-doping impact on the electronic properties of LNIO DPO, we first produced the spin-polarized total density of states (TDOS) for undoped LNIO material in Fig. 4a to provide a frame of reference. One can see that system exhibits an insulating behavior with an E_g of 0.20/2.25

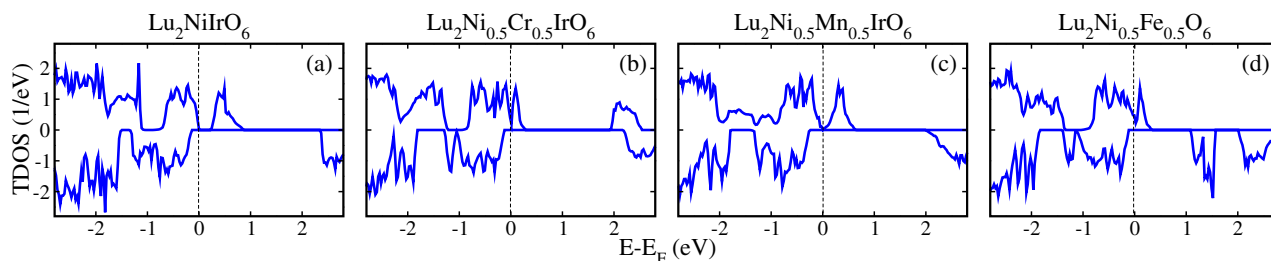


Figure 4. Calculated spin-polarized total density of states (TDOS) within a GGA + U method for (a) undoped $\text{Lu}_2\text{NiIrO}_6$, (b) Cr-doped $\text{Lu}_2\text{NiIrO}_6$ ($\text{Lu}_2\text{Ni}_{0.5}\text{Cr}_{0.5}\text{IrO}_6$), (c) Mn-doped $\text{Lu}_2\text{NiIrO}_6$ ($\text{Lu}_2\text{Ni}_{0.5}\text{Mn}_{0.5}\text{IrO}_6$), and (d) Fe-doped $\text{Lu}_2\text{NiIrO}_6$ ($\text{Lu}_2\text{Ni}_{0.5}\text{Fe}_{0.5}\text{IrO}_6$) double perovskite oxides in a FiM-I spin ordering. The vertical dotted line represents the Fermi level in each DOS case.

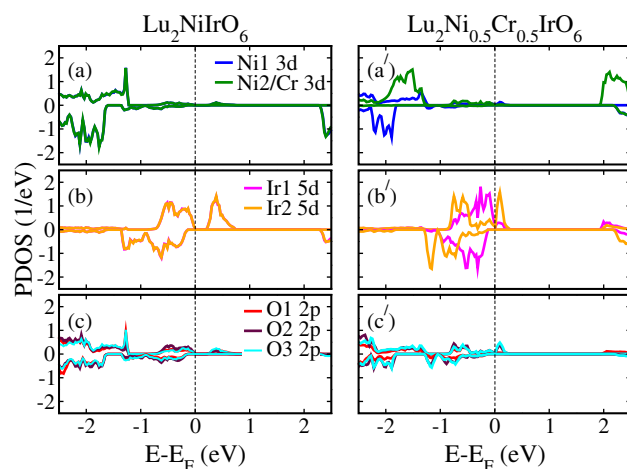


Figure 5. Calculated spin-polarized partial density of states (PDOS) within a GGA + U method for (a/a') Ni and Ni2/Cr 3d, (b/b') Ir1/Ir2 5d, and (c/c') O1/O2/O3 2p orbitals in undoped $\text{Lu}_2\text{NiIrO}_6$ (left column) and Cr-doped $\text{Lu}_2\text{NiIrO}_6$ ($\text{Lu}_2\text{Ni}_{0.5}\text{Cr}_{0.5}\text{IrO}_6$; right column) double perovskite oxides.

eV in the spin-majority/spin-minority channel, which is in good agreement with experimental¹⁸ and previous theoretical work³⁰. Next, we studied the TM-doping influence on the electronic structure of LNIO which exhibits substantial changes. For this, spin-polarized TDOS for Cr, Mn, and Fe-doped LNIO systems are plotted in Fig. 4b–d, respectively, where all the doped materials showing the HM behavior in which the spin-majority channel is conductor while the spin-minority channel is an insulator.

To elucidate the origin of the metallic electronic states in these doped systems, we plotted the spin-polarized partial density of states (PDOS) projected on the Ni/Cr 3d, Ir 5d, and O 2p orbitals in undoped LNIO (left column) and Cr-doped LNIO ($\text{Lu}_2\text{Ni}_{0.5}\text{Cr}_{0.5}\text{IrO}_6$; right column) DPO in Fig. 5, for example. Our calculations clearly show that both 3d states of Ni ions stay away from the Fermi level (E_F) in undoped LNIO material (see Fig. 5a), while Ir 5d states grow around E_F in both valence and conduction bands (Fig. 5b) with small contributions from O 2p states (Fig. 5c). Furthermore, the PDOS analysis in undoped LNIO material indicates that Ni1 and Ni2 3d spin-polarized states are overlapped which means that both ions are showing equivalent contributions to the electronic structure. A similar trend of PDOS can also be seen for Ir and oxygen ions. In the case of Cr-doped LNIO ($\text{Lu}_2\text{Ni}_{0.5}\text{Cr}_{0.5}\text{IrO}_6$) material, Ni/Cr 3d states lie very below and above the E_F in the valence and conduction bands (Fig. 5a'), respectively and not contributing to the metallicity as found in the case of undoped one. Interestingly, Ir 5d states substantially shift from valence to conduction band by crossing E_F in the spin majority channel and are primarily responsible for metallicity with a significant contribution from Ir1 5d states (see Fig. 5b'). A small contribution of O 2p states to the metallicity in the spin majority channel is also evident as displayed in Fig. 5c'. In contrast, an insulating behavior is established in the spin-minority channel for each PDOS as found in the case of undoped one. Hence, with the metallic electronic state in the spin-majority channel and an insulating in the spin-minority channel, the $\text{Lu}_2\text{Ni}_{0.5}\text{Cr}_{0.5}\text{IrO}_6$ material is predicted to be an HM. Here it is very important to note that Ir1 PDOS tends towards degeneracy, which means that it is close to non spin-polarized state having an almost negligible magnetic moment (discuss below). A similar PDOS behavior is also found in the case of Mn- and Fe-doped systems ($\text{Lu}_2\text{Ni}_{0.5}\text{Mn}_{0.5}\text{IrO}_6$ and $\text{Lu}_2\text{Ni}_{0.5}\text{Fe}_{0.5}\text{IrO}_6$) as shown in Figs. 1S and 2S of the Supporting Information (SI), respectively.

For a more deep understanding of the origin of metallic electronic states near E_F , we produced the orbital-resolved PDOS on Ni/Cr/Ir 3d/3d/5d orbitals in undoped LNIO (left column) and Cr-doped LNIO

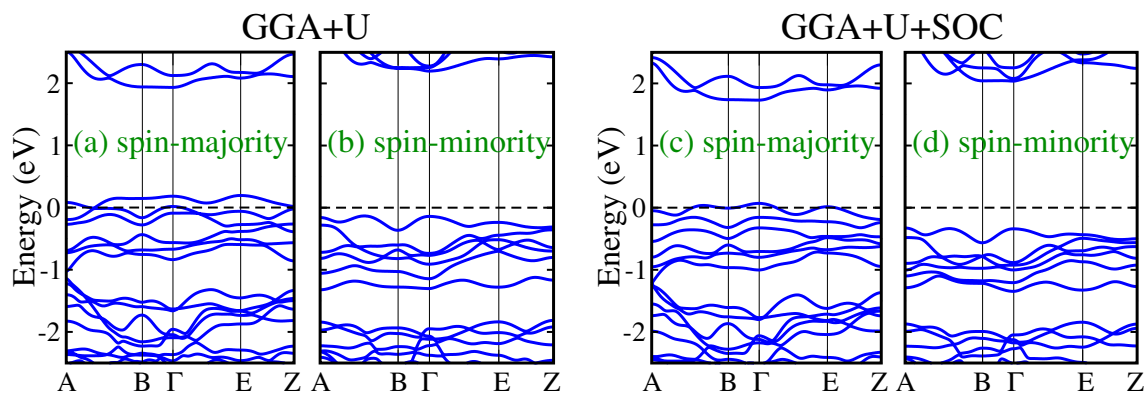


Figure 6. Calculated spin-polarized (a/c) spin-majority and (b/d) spin-minority band structures within GGA + U /GGA + U + SOC method in Cr-doped $\text{Lu}_2\text{Ni}_{0.5}\text{Cr}_{0.5}\text{IrO}_6$ ($\text{Lu}_2\text{Ni}_{0.5}\text{Cr}_{0.5}\text{IrO}_6$) double perovskite oxide.

($\text{Lu}_2\text{Ni}_{0.5}\text{Cr}_{0.5}\text{IrO}_6$; right column) systems in Fig. 3S of the SI. It is very well established that the crystal field splits the d orbitals into low energy triply t_{2g} (d_{xy} , d_{xz} , and d_{yz}) and high energy doubly e_g ($d_{x^2-y^2}$ and $d_{3z^2-r^2}$) states. Moreover, the tetrahedron distortion from perfect order reduces the O_h symmetry to D_{4h} and finally lifts the orbital degeneracy. Hence, the t_{2g} further splits into singlet d_{xy} , d_{xz} , and d_{yz} non-degenerate states. Similarly, the e_g is also divided into singlet $d_{x^2-y^2}$ and $d_{3z^2-r^2}$ non-degenerate states. From Fig. 3S(a) and 3S(b) of the SI, one can see that Ni1 and Ni2 3d orbitals lie away from the E_F in undoped case, respectively. However, the admixture of Ir1 and Ir2 5d orbitals are dominant in both valence and conduction bands, see Fig. 3S(c,d), respectively. It is also very clear that a band gap exists between Ir 5d orbitals in undoped LNIO structure, which also confirms the Mott-insulating state of the system. Similarly, Ni and Cr 3d orbitals are almost showing the negligible contributions around E_F in Cr-doped LNIO system as display in the Fig. 3S(a') and 3S(b') of the SI. Interestingly, the admixture of Ir1 (Fig. 3S(c')) and Ir2 (Fig. 3S(d')) 5d orbitals in the spin-majority channel are crossing the E_F from the valence to conduction bands and are responsible for metallicity. However, the spin minority channels are exhibiting the insulating behavior, which results in the HM state of the system in Cr-doped LNIO system.

For direct observation of the metallic electronic states in doped systems, we plotted the spin-polarized band structures along with the high symmetry directions of the monoclinic Brillouin zone for $\text{Lu}_2\text{Ni}_{0.5}\text{Cr}_{0.5}\text{IrO}_6$ material within both GGA + U (left column) and GGA + U + SOC (right column) methods in Fig. 6, for instance. One can see that in the spin-majority channel, bands grow at the E_F and exhibits metallic behavior as displayed in Fig. 6a within GGA + U scheme. On the other hand, the spin-minority channel shows an insulating nature having an energy gap of 2.32 eV. Hence, the spin majority bands are partially occupied, therefore, an HM state is formed which also confirms the calculated TDOS in Fig. 4b. Contrarily, a considerable downshift in the spin-majority and spin-minority bands are evident with the inclusion of SOC as compared to GGA + U method, compare the Fig. 6c,d with Fig. 6a,b, respectively. However, still a few spin-majority bands are crossing the E_F from valence to conduction channel for GGA + U + SOC calculations (see Fig. 6c), while spin-minority channel remains insulator (see Fig. 6d). Hence one can conclude that despite the down shift of the bands within the GGA + U + SOC method, the HM state of the doped system remains the same as found in the case of GGA + U (without SOC) scheme.

To understand the physical mechanism behind the metallic behavior in these doped materials, we analyze the electronic configurations of ions in each case. In undoped LNIO, Ni is in +2 state with a $3d^8$ configuration which indicates that t_{2g} and e_g states are fully and partially occupied, respectively. This means that three electrons lie in the spin-majority and three in the spin-minority channels of t_{2g} states (i.e., $t_{2g}^3 \uparrow$ and $t_{2g}^3 \downarrow$). The remaining two electrons partially filled the e_g states of the spin-majority channel as $e_g^2 \uparrow e_g^0 \downarrow$. Thus, t_{2g} states completely remain in the valence band, while two up-filled and two down(dn)-empty states of e_g reside in the valence and conduction bands, respectively. Similarly, Ir is in a +4 state having a configuration of $5d^5$ in which t_{2g} and e_g states are partially and empty, respectively. Five electrons of Ir ion are distributed as: three and two electrons lie in the spin-majority and spin-minority channels of t_{2g} states ($t_{2g}^3 \uparrow t_{2g}^2 \downarrow$), respectively. Hence, five (i.e., three up and two dn) states of Ir t_{2g} reside in the valence band and remaining shifts in the conduction region. On the other hand, all the Ir e_g states remain in the conduction band. The schematic representation of electronic configurations for $\text{Ni}^{+2} 3d^8$ and $\text{Ir}^{+4} 5d^5$ orbitals are shown in Fig. 7a,b, respectively.

For $\text{Lu}_2\text{Ni}_{0.5}\text{Cr}_{0.5}\text{IrO}_6$ doped material, Cr is in +3 state with a $3d^3$ configuration and produces a deficiency of five electrons when substituted at $\text{Ni}^{+2} 3d^8$ sites. Hence, the hole was created due to a lack of electrons, therefore, E_F shifts towards lower energies, and few bands crossing the E_F from the valence to the conduction band. This results in a metallic state in the spin-majority channel, while a large band gap still exists in the spin-minority channel which leads the system into an HM state (see Fig. 4b). Similarly, Mn lies in +3 state having $3d^4$ configurations and the system lacks four electrons when it is replaced with $\text{Ni}^{+2} 3d^8$ ions. Hence, e_g states in the spin-majority channel will become fully unoccupied and E_F shifts towards lower energies. Thus, few bands near E_F in the spin-majority channel crossing the E_F which result in a metallicity. On the other hand, the spin-minority channel remains insulator, which leads the system into an HM state (see Fig. 4c). Finally, Fe is also in +3 state with a configuration of $3d^5$ which produces a deficiency of three electrons when it replaced with $\text{Ni}^{+2} 3d^8$ ion, which drags the system into HM state (see Fig. 4d) as discussed above.

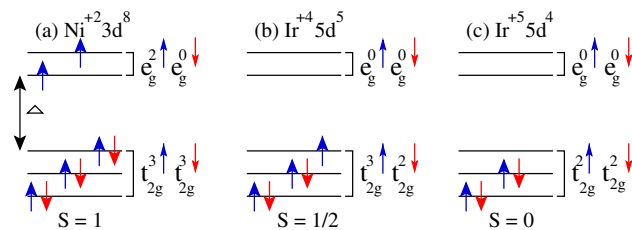


Figure 7. Schematic representation of (a) $\text{Ni}^{+2} 3d^8$, (b) $\text{Ir}^{+4} 5d^5$, and (c) $\text{Ir}^{+5} 5d^4$ orbital configurations.

Magnetism. Next, we examined the calculated total/atom-resolved partial spin magnetic moments in undoped and TM-doped LNIO systems. As allocated in Table 1, the calculated total spin magnetic moments of 1.90(0.95), 4.0(2.0), 5.0(2.5), and 6.0(3.0) μ_B per unit cell(per formula unit) for undoped, Cr-, Mn-, and Fe-doped LNIO materials, respectively. The integral moments per unit cell in all three doped systems affirm the HM state. For the undoped system, the calculated $m_{tot.}$ of 0.95 μ_B /f.u. is almost two times of the experimentally observed value of 0.52 μ_B /f.u.¹⁸. This overestimation is because antisite disorder is not taken into the account in the calculations. As it is theoretically found that when antisite disorder was considered in LNIO system¹⁸, the $m_{tot.}$ was 0.78 μ_B /f.u. which is impending to the experimentally observed value of 0.52 μ_B /f.u. at a very low temperature of 5 K. This shows that Ni and Ir ions remain in +2 and +4 states having electronic configurations of $t_{2g}^3 \uparrow t_{2g}^3 \downarrow e_g^2 \uparrow e_g^0 \downarrow$ and $t_{2g}^3 \uparrow t_{2g}^2 \downarrow e_g^0 \uparrow e_g^0 \downarrow$ with spin states of $S = 1$ and $S = 1/2$, respectively. Moreover, the computed partial spin magnetic moments on Ni and Ir ions are 1.66 and $-0.54 \mu_B$, respectively which means that the Ni ion mainly contributing to $m_{tot.}$. The “-” sign in the Ir moment indicates that its spin is anti-align to that of the Ni. This confirms the strong AFM superexchange coupling between Ni^{+2} and Ir^{+4} ions via oxygen ($\text{Ni}^{+2}\text{-O}^{2-}\text{-Ir}^{+4}$) which results in a FiM ordering.

In the case of doped materials, Ni moment magnitude almost remains the same ($\sim 1.66 \mu_B$) as found in the case of undoped one (Table 1), which means that it remains in a +2 state. However, a strong reduction in the Ir1 spin magnetic moment is found as compared to the undoped one along with a small decrease in the Ir2 moment is also predicted. The computed spin moments on the Ir1/Ir2 are $-0.54/-0.54$, $-0.09/-0.39$, $-0.16/-0.41$, and $-0.05/-0.42$ in undoped LNIO, doped $\text{Lu}_2\text{Ni}_{0.5}\text{Cr}_{0.5}\text{IrO}_6$, $\text{Lu}_2\text{Ni}_{0.5}\text{Mn}_{0.5}\text{IrO}_6$, and $\text{Lu}_2\text{Ni}_{0.5}\text{Fe}_{0.5}\text{IrO}_6$, respectively. This shows that Ir ion lies in a mixed-valence state of +4 and +4/+5 with the configurations of $5d^5 (t_{2g}^3 \uparrow t_{2g}^2 \downarrow)$ and $5d^5/5d^4 (t_{2g}^3 \uparrow t_{2g}^2 \downarrow / t_{2g}^2 \uparrow t_{2g}^2 \downarrow)$ in undoped and all doped structures, respectively. The schematic representation of Ir in +5 state having a configuration of $5d^4 (t_{2g}^2 \uparrow t_{2g}^2 \downarrow)$ with $S = 0$ is shown in Fig. 7c. The individual spin magnetic moments on Cr, Mn, and Fe ions are 2.66, 3.80, and 4.11 μ_B , respectively. Besides the spin moments on the TM and Ir ion sites, the oxygen ions at non-equivalent sites are also spin-polarized (see Table 1) and a sizable spin moment of $\sim -0.40 \mu_B$ arises on the O2 atom in each doped case (see Table 1). Because, a strong hybridization between TM/Ir and oxygen atoms, results in a partial charge transfer from TM (i.e., Cr, Mn, and Fe) and Ir ions to oxygen.

To understand the charge transfer mechanism, we plotted the spin-magnetization density isosurface plots for undoped and Cr-doped ($\text{Lu}_2\text{Ni}_{0.5}\text{Cr}_{0.5}\text{IrO}_6$) materials in Fig. 8a,b, respectively. As one can see in the undoped case (Fig. 8a), Ni 3d and Ir 5d orbitals are primarily contributing to the spin density. It is a well-known fact that Ni is in +2 state with a d^8 configuration in LNIO. Thus, the t_{2g} (d_{xy} , d_{yz} , and d_{xz}) states are fully occupied by maintaining six electrons, while the remaining two unpaired electrons lie in the e_g ($d_{x^2-y^2}$ and $d_{3z^2-r^2}$) states. Therefore, the e_g orbital characteristics are visible in the isosurfaces of the Ni ions in both undoped and Cr-doped LNIO materials as displayed in Fig. 8a,b, respectively. Moreover, very small spin densities have also appeared on the oxygen atoms. Because of a small charge transfer on the oxygen ions due to superexchange coupling between Ni^{+2} and Ir^{+4} ions via oxygen ($\text{Ni}^{+2}\text{-O}^{2-}\text{-Ir}^{+4}$). Interestingly, substantial changes occur in the magnitude of spin densities when one of the Ni ions is replaced with Cr, see Fig. 8b. The most striking feature of the present calculations is that spin-density around Ir1 ion is almost disappeared, while a small decrease in Ir2 is evident which confirms the calculated spin magnetic moments on Ir ions in Cr-doped LNIO system in Table 1. Moreover, the spin density nature of Cr ion is due to the admixture of d_{xy} , d_{yz} , and d_{xz} (i.e., t_{2g}) orbitals character. Besides, a substantial amount of spin density arises on the oxygen ions in Cr-doped (Fig. 8b) system than that of undoped one (Fig. 8a), because extra charge transfer from Ni/Cr and Ir ions to oxygen due to strong hybridization between them.

Conclusion

Employing non-degenerate DFT calculations, the electronic and magnetic properties of undoped and transition metal (TM) = Cr, Mn, and Fe-doped $\text{Lu}_2\text{NiIrO}_6$ double perovskite oxides are investigated, where TM ions having 50% concentration are substituted at Ni-site. We found that the undoped material is a ferrimagnetic (FiM) Mott-insulator, while all the doped structures exhibit half-metallic FiM behavior. The metallic electronic states in the spin majority channels mainly belong to the admixture of Ir 5d orbitals in each case. It is also established that Ir ion lies in a mixed-valence state of +4 and +5 in all doped systems with configurations of $5d^5 (t_{2g}^3 \uparrow t_{2g}^2 \downarrow)$ and $5d^4 (t_{2g}^2 \uparrow t_{2g}^2 \downarrow)$, respectively, which results in a strong reduction of magnetic moment on the Ir $5d^4$ ion. Interestingly, our calculations revealed that structural distortion enhanced when one of the Ni ions is replaced with TM, and maximum deviation from the perfect cubic symmetry is obtained in the case of the Cr-doped

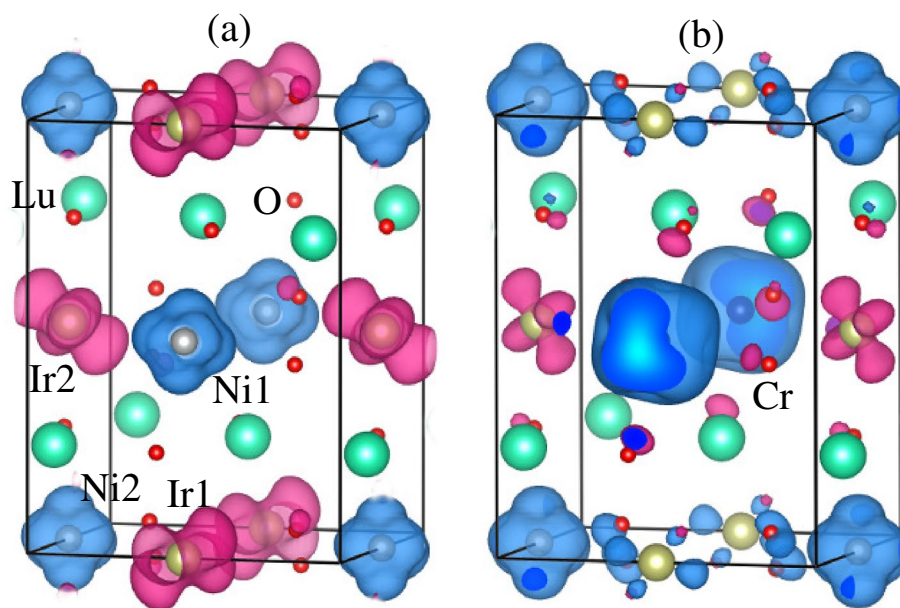


Figure 8. Spin-magnetization density isosurface plots for (a) undoped and (b) Cr-doped $\text{Lu}_2\text{NiIrO}_6$ ($\text{Lu}_2\text{Ni}_{0.5}\text{Cr}_{0.5}\text{IrO}_6$) materials at the same iso-value of $\pm 0.04 \text{ e}/\text{\AA}^3$. The light blue and light pink colors represent the spin up and spin down states, respectively.

$\text{Lu}_2\text{NiIrO}_6$ material, which further optimize the FiM ordering temperature. Therefore, $\text{Lu}_2\text{Ni}_{0.5}\text{Cr}_{0.5}\text{IrO}_6$ system exhibits a higher FiM ordering temperature of 292 K as compared to undoped and other doped systems. Hence, these doped materials show promise of their probable feasible applications in hard magnetic memory devices.

Computational methods

First-principles electronic structure calculations based on DFT were performed using a full-potential linearized augmented plane wave method as implemented in the WIEN2K code⁵⁸. The exchange-correlation functional which is parameterized by generalized gradient approximation (GGA)⁵⁹ plus on-site Coulomb interaction (GGA+ U) approach was employed with $U = 3.85, 3.5, 4.0, 5.0, 5.1,$ and 2.8 eV for Lu $4f$, Cr $3d$, Mn $3d$, Fe $3d$, Ni $3d$, and Ir $5d$ states, respectively⁶⁰. In all cases, the spin non-degenerate version of the GGA is utilized for both with and without SOC calculations. The relativistic (i.e., SOC) effects attributed with spin-magnetization align along the [100], [010], [001], [110], [101], [011], and [111] directions and found that [001] axis is the easy axis. For the wave function expansion inside the atomic spheres, a maximum value of $l_{max} = 12$ is chosen and the plane-wave cutoff is set to $R_{mt} \times K_{max} = 7$ with $G_{max} = 24$. A $7 \times 7 \times 9$ k -space grid with 128 points within the irreducible wedge of the Brillouin zone is found to be well converged. Along with this, full relaxation of the atomic positions by minimizing the atomic forces up to 2 mRy/a.u. is taken into account in each case. Self-consistency is assumed for a total energy convergence of less than 10^{-5} Ry .

Received: 24 September 2020; Accepted: 18 December 2020

Published online: 13 January 2021

References

- Kobayashi, K. I., Kimura, T., Sawada, H., Terakura, K. & Tokura, Y. Room-temperature magnetoresistance in an oxide material with an ordered double-perovskite structure. *Nature* **395**, 677. <https://doi.org/10.1038/27167> (1998).
- Kobayashi, K.-I. *et al.* Intergrain tunneling magnetoresistance in polycrystals of the ordered double perovskite $\text{Sr}_2 \text{FeMoO}_6$. *Phys. Rev. B* **59**, 11159–11162. <https://doi.org/10.1103/PhysRevB.59.11159> (1999).
- Maignan, A., Raveau, B., Martin, C. & Hervieu, M. Large intragrain magnetoresistance above room temperature in the double perovskite $\text{Ba}_2 \text{FeMoO}_6$. *J. Solid State Chem.* **144**, 224–227. <https://doi.org/10.1006/jssc.1998.8129> (1999).
- Kim, T. H., Uehara, M., Cheong, S. W. & Lee, S. Large room-temperature intergrain magnetoresistance in double perovskite $\text{SrFe}_{1-x}(\text{Mo or Re})_x \text{O}_3$. *Appl. Phys. Lett.* **74**, 1737–1739. <https://doi.org/10.1063/1.123672> (1999).
- Arevalo-Lopez, A. M., McNally, G. M. & Attfield, J. P. Large magnetization and frustration switching of magnetoresistance in the double-perovskite ferrimagnet $\text{Mn}_2 \text{FeReO}_6$. *Angew. Chem. Int. Ed.* **54**, 12074–12077. <https://doi.org/10.1002/anie.201506540> (2015).
- Li, M.-R. *et al.* Giant magnetoresistance in the half-metallic double-perovskite ferrimagnet $\text{Mn}_2 \text{FeReO}_6$. *Angew. Chem. Int. Ed.* **54**, 12069–12073. <https://doi.org/10.1002/anie.201506456> (2015).
- Tomioka, Y. *et al.* Magnetic and electronic properties of a single crystal of ordered double perovskite $\text{Sr}_2 \text{FeMoO}_6$. *Phys. Rev. B* **61**, 422–427. <https://doi.org/10.1103/PhysRevB.61.422> (2000).
- Kato, H., Okuda, T., Okimoto, Y. & Tomioka, Y. Metallic ordered double-perovskite $\text{Sr}_2 \text{CrReO}_6$ with maximal curie temperature of 635 K. *Appl. Phys. Lett.* **81**, 328. <https://doi.org/10.1063/1.1493646> (2002).

9. Kato, H. *et al.* Structural and electronic properties of the ordered double perovskites A_2M ReO₆ (A=Sr, Ca; M=Mg, Sc, Cr, Mn, Fe Co, Ni, Zn). *Phys. Rev. B* **69**, 184412. <https://doi.org/10.1103/PhysRevB.69.184412> (2004).
10. Feng, H. L. *et al.* High-temperature ferrimagnetism driven by lattice distortion in double perovskite Ca₂ FeOsO₆. *J. Am. Chem. Soc.* **136**, 3326–3329. <https://doi.org/10.1021/ja411713q> (2014).
11. Philipp, J. B. *et al.* Structural and doping effects in the half-metallic double perovskite A₂ CrWO₆ (A = Sr, Ba, and Ca). *Phys. Rev. B* **68**, 144431. <https://doi.org/10.1103/PhysRevB.68.144431> (2003).
12. Samanta, K., Sanyal, P. & Saha-Dasgupta, T. Half-metallic behavior in doped Sr₂ CrOsO₆ double perovskite with high transition temperature. *Sci. Rep.* **5**, 15010. <https://doi.org/10.1038/srep15010> (2015).
13. Retuerto, M. *et al.* Half-metallicity in Pb₂ CoReO₆ double perovskite and high magnetic ordering temperature in Pb₂ CrReO₆ perovskite. *Chem. Mater.* **27**, 4450–4458. <https://doi.org/10.1021/acs.chemmater.5b01442> (2015).
14. Muller, G. M. *et al.* Half-metallic ferromagnets: From band structure to many-body effects. *Nat. Mater.* **8**, 56. <https://doi.org/10.1038/nmat2341> (2009).
15. Krockenberger, Y. *et al.* A neutron scattering study of the crystal and magnetic structure of Sr₂ CrOsO₂. *J. Magn. Magn. Mater.* **310**, 1854. <https://doi.org/10.1016/j.jmmm.2006.10.648> (2007).
16. Krockenberger, Y. *et al.* Sr₂ CrOsO₂: End point of a spin-polarized metal-insulator transition by 5d band filling. *Phys. Rev. B* **75**, 020404. <https://doi.org/10.1103/PhysRevB.75.020404> (2007).
17. Feng, H. L. *et al.* Ba₂ NiOsO₆: A dirac-mott insulator with ferromagnetism near 100 k. *Phys. Rev. B* **94**, 235158. <https://doi.org/10.1103/PhysRevB.94.235158> (2016).
18. Feng, H. L. *et al.* High-pressure synthesis of Lu₂ NiIrO₆ with ferrimagnetism and large coercivity. *Inorg. Chem.* **58**, 397–404. <https://doi.org/10.1021/acs.inorgchem.8b02557> (2019).
19. Shimakawa, Y., Azuma, M. & Ichikawa, N. Multiferroic compounds with double-perovskite structures. *Materials* **4**, 153–168. <https://doi.org/10.3390/ma4010153> (2011).
20. Feng, H. L. *et al.* High-temperature ferrimagnetism with large coercivity and exchange bias in the partially ordered 3d/5d hexagonal perovskite Ba₂ Fe_{1.12} Os_{0.88} O₆. *Chem. Mater.* **29**, 886–895. <https://doi.org/10.1021/acs.chemmater.6b04983> (2017).
21. Rogado, N., Li, J., Sleight, A. & Subramanian, M. Magnetocapacitance and magnetoresistance near room temperature in a ferromagnetic semiconductor: La₂ NiMnO₆. *Adv. Mater.* **17**, 2225–2227. <https://doi.org/10.1002/adma.200500737> (2005).
22. Sarma, D. D., Mahadevan, P., Saha-Dasgupta, T., Ray, S. & Kumar, A. Electronic structure of Sr₂ FeMoO₆. *Phys. Rev. Lett.* **85**, 2549–2552. <https://doi.org/10.1103/PhysRevLett.85.2549> (2000).
23. Solovyev, I. V. Electronic structure and stability of the ferrimagnetic ordering in double perovskites. *Phys. Rev. B* **65**, 144446. <https://doi.org/10.1103/PhysRevB.65.144446> (2002).
24. Jeng, H.-T. & Guo, G. Y. First-principles investigations of orbital magnetic moments and electronic structures of the double perovskites Sr₂ FeMoO₆, Sr₂ FeReO₆, and Sr₂ CrWO₆. *Phys. Rev. B* **67**, 094438. <https://doi.org/10.1103/PhysRevB.67.094438> (2003).
25. Felser, C., Fecher, G. & Balke, B. Spintronics: A challenge for materials science and solid-state chemistry. *Angew. Chem. Int. Ed.* **46**, 668–699. <https://doi.org/10.1002/anie.200601815> (2007).
26. Katsnelson, M. I., Irkhin, V. Y., Chioncel, L., Lichtenstein, A. & de Groot, R. A. Half-metallic ferromagnets: From band structure to many-body effects. *Rev. Mod. Phys.* **80**, 315. <https://doi.org/10.1103/RevModPhys.80.315> (2008).
27. Shibata, G. *et al.* Anisotropic spin-density distribution and magnetic anisotropy of strained La_{1-x} Sr_x MnO₃ thin films: Angle-dependent x-ray magnetic circular dichroism. *Rev. Mod. Phys.* **3**, 3. <https://doi.org/10.1038/s41535-018-0077-4> (2018).
28. Asano, H., Kozuka, N., Tsuzuki, A. & Matsui, M. Growth and properties of high-curie-temperature Sr₂ CrReO₆ thin films. *Appl. Phys. Lett.* **85**, 263. <https://doi.org/10.1063/1.1769085> (2004).
29. Majewski, P., Geprgs, S., Sanganas, O., Opel, M. & Gross, R. X-ray magnetic circular dichroism study of Re 5d magnetism in Sr₂ CrReO₆. *Appl. Phys. Lett.* **87**, 202503. <https://doi.org/10.1063/1.2131178> (2005).
30. Nazir, S. Ferri-magnetic mott-insulating state in Lu₂ NiIrO₆: Ab-initio study. *J. Alloys Compd.* **835**, 155351. <https://doi.org/10.1016/j.jallcom.2020.155351> (2020).
31. Navarro, J. *et al.* Antisite defects and magnetoresistance in Sr₂ FeMoO₆ double perovskite. *J. Phys. Condens. Matter* **13**, 8481–8488. <https://doi.org/10.1088/0953-8984/13/37/305> (2001).
32. Rubi, D. *et al.* Spectroscopic investigation on the influence of AS defects on the electronic structure of Sr₂ FeMoO₆. *J. Phys. Chem. Solids* **67**, 575. <https://doi.org/10.1016/j.jpcs.2005.10.123> (2006).
33. Linden, J., Shimada, T., Motohashi, T., Yamauchi, H. & Karppinen, M. Iron and molybdenum valences in double-perovskite (Sr, Nd)₂ FeMoO₆: Electron-doping effect. *Sol. State Commun.* **129**, 129–133. <https://doi.org/10.1016/j.ssc.2003.09.025> (2004).
34. Hemery, E. K., Williams, G. V. M. & Trodahl, H. J. La-induced changes in the magnetic and electronic properties of Sr_{2-x} La_{1-x} FeMoO₆. *Phys. Rev. B* **74**, 054423. <https://doi.org/10.1103/PhysRevB.74.054423> (2006).
35. Geprags, S., Majewski, P., Gross, R., Ritter, C. & Alff, L. Electron doping in the double perovskite La_x A_{2-x} CrWO₆ with A = Sr and Ca. *J. Appl. Phys.* **99**, 08J102. <https://doi.org/10.1063/1.2167054> (2006).
36. Buřaical, L. *et al.* Physical properties of disordered double-perovskite Ca_{2-x} La_x FeReO₆. *J. Appl. Phys.* **103**, 07F716. <https://doi.org/10.1063/1.2830719> (2008).
37. Blasco, J., Ritter, C., Rodriguez-Velamazan, J. & Herrero-Martin, J. Electron doping versus antisite defects: Structural and magnetic properties of Sr_{2-x} La_x CrMoO₆ and Sr_{2-x} La_x Cr_{1+x/2} Mo_{1-x/2} O₆ perovskites. *Solid State Sci.* **12**, 750–758. <https://doi.org/10.1016/j.solidstatesciences.2010.02.025> (2010).
38. Buřaical, L. *et al.* Structural, electronic and magnetic properties of the series of double perovskites (Ca, Sr)_{2-x} La_x FeIrO₆. *J. Solid State Chem.* **212**, 23–29. <https://doi.org/10.1016/j.jssc.2014.01.007> (2014).
39. Zu, N., Wang, J. & Wu, Z. Pressure-induced half-metallic ferrimagnetism in La₂ VMnO₆. *J. Phys. Chem. C* **117**, 7231–7235. <https://doi.org/10.1021/jp3118538> (2013).
40. Coutrim, L. T. *et al.* Structural and magnetic properties of the La_{2-x} Ca_x CoIrO₆ double perovskite series. *J. Solid State Chem.* **221**, 373–377. <https://doi.org/10.1016/j.jssc.2014.10.019> (2015).
41. Huo, G., Ding, L. & Li, Z. Structural, magnetic and transport properties of S doping in Sr₂ FeMoO₆ compound. *Solid State Sci.* **76**, 85–91. <https://doi.org/10.1016/j.solidstatesciences.2017.12.009> (2018).
42. Wang, H., Zhu, S., Ou, X. & Wu, H. Ferrimagnetism in the double perovskite Ca₂ FeOsO₆: A density functional study. *Phys. Rev. B* **90**, 054406. <https://doi.org/10.1103/PhysRevB.90.054406> (2014).
43. Zu, N. *et al.* Abinitio study on Pb₂ FeOsO₆ and possible half metallicity via Na doping. *J. Magn. Magn. Mater.* **491**, 165553. <https://doi.org/10.1016/j.jmmm.2019.165553> (2019).
44. Lv, S. *et al.* Effect of electron doping on the magnetic properties and electronic structures of Ba₂ MnMoO₆. *J. Alloys Compd.* **774**, 618–624. <https://doi.org/10.1016/j.jallcom.2018.10.014> (2019).
45. Bandyopadhyay, A. *et al.* Evolution of electronic and magnetic properties in a series of iridate double perovskites Pr_{2-x} Sr_x MgIrO₆ (x = 0, 0.5, 1.0). *Phys. Rev. B* **100**, 064416. <https://doi.org/10.1103/PhysRevB.100.064416> (2019).
46. Rout, P. C. & Srinivasan, V. Exploring the structural, electronic, and magnetic properties of cation-ordered 3d-5d double-perovskite Bi₂ FeReO₆ and Bi₂ FeIrO₆ thin films from first principles. *Phys. Rev. B* **100**, 245136. <https://doi.org/10.1103/PhysRevB.100.245136> (2019).
47. Bhandari, S. R. *et al.* Electronic, magnetic, optical, and thermoelectric properties of Ca₂ Cr_{1-x} Ni_x OsO₆ double perovskites. *RSC Adv.* **10**, 16179–16186. <https://doi.org/10.1039/C9RA10775D> (2020).

48. Lu, R. *et al.* The effect of biaxial mechanical strain on the physical properties of double perovskite $\text{Sr}_2\text{FeMoO}_6$: A theoretical study. *Solid State Commun.* **191**, 70. <https://doi.org/10.1016/j.ssc.2014.03.017> (2014).
49. Boeri, L., Dolgov, O. V. & Golubov, A. A. Is $\text{LaFeAsO}_{1-x}\text{F}_x$ an electron-phonon superconductor?. *Phys. Rev. Lett.* **101**, 026403. <https://doi.org/10.1103/PhysRevLett.101.026403> (2008).
50. Macquart, R. *et al.* Synthesis, structure, and magnetic properties of $\text{Sr}_2\text{NiOsO}_6$ and $\text{Ca}_2\text{NiOsO}_6$: Two new Osmium containing double perovskites. *Inorg. Chem.* **44**, 9676–9683 <https://doi.org/10.1021/ic051045+> (2005).
51. Morrow, R. *et al.* Independent ordering of two interpenetrating magnetic sublattices in the double perovskite $\text{Sr}_2\text{CoOsO}_6$. *J. Am. Chem. Soc.* **135**, 18824–18830. <https://doi.org/10.1021/ja407342w> (2013).
52. Morrow, R., Freeland, J. W. & Woodward, P. M. Probing the links between structure and magnetism in $\text{Sr}_{2-x}\text{Ca}_x\text{FeOsO}_6$ double perovskites. *Inorg. Chem.* **53**, 7983–7992. <https://doi.org/10.1021/ic5006715> (2014).
53. Morrow, R. *et al.* Effects of chemical pressure on the magnetic ground states of the osmate double perovskites SrCaCoOsO_6 and $\text{Ca}_2\text{CoOsO}_6$. *Phys. Rev. B* **92**, 094435. <https://doi.org/10.1103/PhysRevB.92.094435> (2015).
54. Gauvin-Ndiaye, C., Tremblay, A.-M.S. & Nourafkan, R. Electronic and magnetic properties of the double perovskites $\text{La}_2\text{MnRuO}_6$ and LaMnFeO_6 ($A = \text{Ba, Sr, Ca}$) and their potential for magnetic refrigeration. *Phys. Rev. B* **99**, 125110. <https://doi.org/10.1103/PhysRevB.99.125110> (2019).
55. Powell, A. V., Gore, J. G. & Battle, P. D. The magnetic properties of iridium in mixed-metal oxides. *J. Alloys Compd.* **201**, 73–84. [https://doi.org/10.1016/0925-8388\(93\)90864-J](https://doi.org/10.1016/0925-8388(93)90864-J) (1993).
56. Currie, R. C., vente, J. F., Frikkee, E. & Igdo, D. J. W. The structure and magnetic properties of $\text{La}_2\text{M}\text{LrO}_6$ with $M = \text{Mg, Co, Ni}$, and Zn . *J. Solid State Chem.* **116**, 199–204. <https://doi.org/10.1006/jssc.1995.1202> (1995).
57. Ferreira, T., Morrison, G., Yeon, J. & zur Loye, H.-C. Design and crystal growth of magnetic double perovskite iridates: $\text{Ln}_2\text{MlIrO}_6$ ($L = \text{La, Pr, Nd, Sm-Gd}$; $M = \text{Mg, Ni}$). *Cryst. Growth Des.* **16**, 2795–2803. <https://doi.org/10.1021/acs.cgd.6b00121> (2016).
58. Blaha, P., Schwarz, K., Sorantin, P. & Trickey, S. B. Full-potential, linearized augmented plane wave programs for crystalline systems. *Comput. Phys. Commun.* **59**, 399. [https://doi.org/10.1016/0010-4655\(90\)90187-6](https://doi.org/10.1016/0010-4655(90)90187-6) (1990).
59. Perdew, J. P., Burke, K. & Ernzerhof, M. Generalized gradient approximation made simple. *Phys. Rev. Lett.* **77**, 3865. <https://doi.org/10.1103/PhysRevLett.77.3865> (1996).
60. Calderon, C. E. *et al.* The aflow standard for high-throughput materials science calculations. *Comput. Mater. Sci.* **108**, 233. <https://doi.org/10.1016/j.commatsci.2015.07.019> (2015).

Acknowledgements

The computational work was supported by University of Sargodha, Sargodha, Pakistan.

Author contributions

S.N. conducted the calculations and also wrote the manuscript.

Competing interests

The author declares no competing interests.

Additional information

Supplementary Information The online version contains supplementary material available at <https://doi.org/10.1038/s41598-020-80265-6>.

Correspondence and requests for materials should be addressed to S.N.

Reprints and permissions information is available at www.nature.com/reprints.

Publisher's note Springer Nature remains neutral with regard to jurisdictional claims in published maps and institutional affiliations.



Open Access This article is licensed under a Creative Commons Attribution 4.0 International License, which permits use, sharing, adaptation, distribution and reproduction in any medium or format, as long as you give appropriate credit to the original author(s) and the source, provide a link to the Creative Commons licence, and indicate if changes were made. The images or other third party material in this article are included in the article's Creative Commons licence, unless indicated otherwise in a credit line to the material. If material is not included in the article's Creative Commons licence and your intended use is not permitted by statutory regulation or exceeds the permitted use, you will need to obtain permission directly from the copyright holder. To view a copy of this licence, visit <http://creativecommons.org/licenses/by/4.0/>.

© The Author(s) 2021